Received: 17 July 2024 | Revised: 25 October 2024 | Accepted: 20 November 2024

DOI: 10.1002/qj.4917

Quarterly Journal of the Royal Meteorological Society RMetS

RESEARCH ARTICLE

A vorticity budget for theoretical and convectively coupled equatorial Rossby waves: Dynamical propagation and growth mechanisms

Adrian J. Matthews

Centre for Ocean and Atmospheric Sciences, School of Environmental Sciences and School of Mathematics, University of East Anglia, Norwich, UK

Correspondence
Adrian J. Matthews, School of Environmental Sciences, University of East Anglia, Norwich, UK.
Email: a.j.matthews@uea.ac.uk

Funding information
Natural Environment Research Council, Grant/Award Number: NE/R016704/1

Abstract

Convectively coupled equatorial Rossby waves (CCERWs) are westward-propagating tropical weather systems that can trigger extreme precipitation and flooding. Here, vorticity budgets are used to determine their dynamical mechanisms of propagation and growth. First, an analytical solution to the vorticity budget of theoretical dry $n = 1$ equatorial Rossby waves is presented. Westward propagation arises entirely from the planetary vorticity advection ($-\beta v$) term, where high-magnitude planetary vorticity is advected equatorward from higher latitudes to the west of cyclonic perturbations in the Rossby-wave structure. This is the classical Rossby-wave propagation mechanism. There is one other non-zero term in the vorticity budget: the vortex stretching ($-fD$) term has a (weak) eastward propagation tendency, mainly due to the convergence in the meridional wind structure to the east of the cyclonic perturbations. This acts to slow the overall westward propagation down. Both these terms are in quadrature with the vorticity structure and hence the theoretical waves are neutral. A vorticity budget of observed CCERWs is then presented, using reanalysis data. The primary westward propagation mechanism is still the planetary vorticity advection term. However, the convergence centres are now aligned with the cyclonic vorticity centres, rather than a quarter cycle to the east. Hence the vortex stretching ($-fD$) term is now in phase with the vorticity, leading to growth of CCERWs. There is an even stronger growth contribution from the nonlinear vortex stretching $-\zeta D$ term. Horizontal vorticity advection and subgrid-scale processes both act to damp the CCERW. The total source term is one of westward propagation and growth. This diagnostic vorticity-budget approach can be applied to inform the assessment of forecast skill and model development.

KEYWORDS

convection, equatorial Rossby wave, growth mechanism, propagation mechanism, vorticity budget

1 | INTRODUCTION

Convectively coupled equatorial Rossby waves (CCERWs) are westward-propagating tropical weather systems that are found ubiquitously in the major tropical convective regions (Takayabu, 1994; Wheeler & Kiladis, 1999). They have a coherent precipitation and dynamical structure associated with them (Wheeler *et al.*, 2000; Yang *et al.*, 2003). CCERWs have a relatively low propagation speed, such that the local precipitation signal can last over one week in a given location. Hence they are a major contributor to precipitation variability on subseasonal time-scales (Tsai *et al.*, 2020) and an important source of subseasonal prediction skill (Dias *et al.*, 2023). In particular, they are important components of subseasonal variability in the major monsoon systems over West Africa (Janicot *et al.*, 2010) and South Asia through the Boreal Summer Intraseasonal Oscillation (Kemball-Cook & Wang, 2001).

Recently, there has been a surge of interest in the role of CCERWs, and convectively coupled equatorial waves in general, in extreme precipitation (Baranowski *et al.*, 2020). This is based on the multi-scale interaction structure of convective systems in the Tropics, where slowly varying, large-scale structures (such as CCERWs) set the environment within which shorter time-scale, smaller spatial scale structures (such as mesoscale convective systems) can develop and produce local extreme precipitation (Meehl *et al.*, 2001). For example, the probability of extreme precipitation increases by a factor of three over eastern Malaysia and the Philippines during the passage of the envelope of convection associated with CCERWs during the northern winter season (Ferrett *et al.*, 2020).

Additionally, CCERWs can also interact nonlinearly with other tropical weather systems. For example, the probability of extreme precipitation and/or flooding in Sulawesi doubles if either a CCERW or a convectively coupled Kelvin wave (CCKW) is present (Latos *et al.*, 2021). If both occur simultaneously, the probability increases by a factor of eight. As well as increasing the probability of extreme precipitation within the large-scale convective envelope, CCERWs can also contribute indirectly to extreme precipitation. During the development of Tropical Cyclone *Seroja*, a moisture supply was provided by a CCERW that advected moist air around its lower tropospheric cyclonic part to feed into the developing tropical cyclone (Latos *et al.*, 2023). In a similar manner, CCERWs have also been linked to cold surges on the western flank of their cyclonic anomalies over the South China Sea, leading to extreme precipitation there (Diong *et al.*, 2023). In general, CCERWs have a well-established link with tropical cyclone genesis (Frank & Roundy, 2006); globally, 60% of pre-tropical cyclogenesis events are associated with CCERW precursors (Feng *et al.*, 2023). The causal mechanism here appears to be an increase in mid-level relative humidity and low-level cyclonic vorticity associated with the CCERW (Zhao & Wu, 2018).

From their inception in the 1990s, CCERWs have implicitly been assumed to be essentially analogues of the westward-propagating theoretical dry equatorial Rossby waves (Matsuno, 1966), modified by moist convection (Kiladis *et al.*, 2009). Similarly, the other classes of theoretical equatorial waves (Kelvin, mixed Rossby–gravity, inertio-gravity) also have their convectively coupled equatorial wave (CCEW) analogues. This assumption is also made in practice, as the two main methods of diagnosing CCEWs in general (Knippertz *et al.*, 2022) use it: (1) the wavenumber–frequency filtering method is based on the dispersion curves of theoretical equatorial waves (Wheeler & Kiladis, 1999); (2) the dynamical structure method is based on projecting wind data onto the meridional dynamical structure of theoretical waves (Yang *et al.*, 2003). The success of both of these methods justifies that assumption.

As is implicit in the name, coupling with convection is key to understanding the mechanisms of CCERWs. Convection within CCERWs is observed to be in phase with the total column water anomaly, and convection in their active region is actually due to triggering of mesoscale interactions (Nakamura & Takayabu, 2022a). Fuchs-Stone *et al.* (2019) postulated that CCERWs are unstable moisture modes, using the Wind-Induced Surface Heat Exchange (WISHE) framework. The phase speed of an initial westward-propagating free equatorial Rossby wave was found to slow down when the wave was coupled with convection, due to WISHE and cloud–radiation interactions. Background easterly shear can also help to destabilise such a westward-propagating moisture mode (Chen, 2022). The interactions between convection and dynamics and the related thermodynamical mechanisms are crucial to understand the propagation and growth of convectively coupled equatorial waves, including CCERWs.

However, insights can also be gained by examining the purely dynamical balances within such waves. Such an analysis was recently carried out for CCKWs (Matthews, 2021). Here, a vorticity-budget analysis was performed for both theoretical equatorial Kelvin waves and observed CCKWs. The dynamical eastward propagation of the CCKW could be accounted for as a modified version of the vorticity balance within the theoretical Kelvin wave. Hence, although the overall general structure of CCERWs has been well documented, their vorticity and related divergence structures are not well known.

The purpose of this article is to establish the dynamical mechanisms of propagation and growth of observed CCERWs and to compare them with those same

mechanisms in theoretical equatorial Rossby waves. It is intended as a follow-on article to Matthews (2021). The main hypothesis to be tested is that the CCERW acts dynamically like a modified dry equatorial Rossby wave. It is anticipated that the main westward propagation mechanism will still be the standard Rossby-wave mechanism of meridional advection of planetary vorticity, but that this will be modified by the addition of other vorticity source terms. A further hypothesis is that there will be vorticity source terms that will enable the CCERW to grow, in contrast to theoretical equatorial Rossby waves, which are neutral waves with zero growth.

The study region will be the Indian Ocean. CCERWs occur throughout the Tropics, but the Indian Ocean is a large, mainly homogeneous ocean basin, where convection can occur over a wide range of tropical latitudes. All other tropical regions will introduce confounding factors that may mask the propagation and growth regions of CCERWs. Over Africa and South America, land–atmosphere interactions and moisture availability will likely be a complicating factor. Over the Maritime Continent, the complex geometry of large islands and shallow seas will also add a layer of complexity. The Pacific Ocean is also a large ocean basin, but convection is limited over much of it to a narrow Intertropical Convergence Zone (ITCZ) to the north of the Equator, restricting convection to a limited latitude domain and complicating analysis of the underlying mechanisms. Finally, the Atlantic also suffers from the ITCZ problem and is also relatively longitudinally narrow.

2 | THEORETICAL LINEAR EQUATORIAL ROSSBY WAVE

In Section 2.1, the structure of theoretical equatorial Rossby waves is summarised, following, for example, Matsuno (1966) and Gill (1982). This is followed in Section 2.2 by an analysis of the dynamical propagation and growth mechanisms of these theoretical equatorial Rossby waves using a vorticity-budget approach, following Matthews (2021).

2.1 | Equatorial Rossby-wave dynamical structure

The equations of motion are linearised about a background atmosphere of zero motion, leading to a separation of variables into two systems: (1) a vertical structure equation giving the vertical structure (e.g., first internal mode) and (2) the shallow-water equations governing the horizontal and time structure. The shallow-water equations on an equatorial beta plane ($f = \beta y$), with zonal wind speed $u(x,y,t)$, meridional wind speed $v(x,y,t)$, geopotential height $Z(x,y,t)$, are

$$\frac{\partial u}{\partial t} - \beta y v = -g\frac{\partial Z}{\partial x}, \qquad \frac{\partial v}{\partial t} + \beta y u = -g\frac{\partial Z}{\partial y},$$
$$g\frac{\partial Z}{\partial t} + c_e^2\left(\frac{\partial u}{\partial x} + \frac{\partial v}{\partial y}\right) = 0. \tag{1}$$

Here, x is distance eastward, y is distance northward from the Equator, t is time, $\beta = 2.3 \times 10^{-11}\ \mathrm{m^{-1} \cdot s^{-1}}$ is the northward gradient of planetary vorticity, $g = 9.81\ \mathrm{m \cdot s^{-2}}$ is the acceleration due to gravity, and c_e is the gravity-wave speed of the solutions and is related to the separation constant at the separation of variables step above.

The solutions can be separated further, in the form

$$u(x,y,t) = \hat{u}(y)e^{i(kx-\omega t)}, \qquad v(x,y,t) = \hat{v}(y)e^{i(kx-\omega t)},$$
$$Z(x,y,t) = \hat{Z}(y)e^{i(kx-\omega t)}, \tag{2}$$

where the $\hat{u}$, $\hat{v}$, and $\hat{Z}$ variables contain the (unknown) y structures of the solutions and the x and t structures are combined into a travelling wave with wavenumber k in the x direction and frequency ω. A single ordinary differential equation can then be obtained for $\hat{v}$. The solutions are parabolic cylinder functions, and the dispersion relation is

$$\frac{c_e}{\beta}\left(\frac{\omega^2}{c_e^2} - k^2 - \frac{\beta k}{\omega}\right) = 2n + 1, \tag{3}$$

where n is any positive integer. The solution for the physically important $n = 1$ equatorial Rossby wave is

$$\hat{v}(y) = 2v_0\left(\frac{\beta}{c_e}\right)^{1/2} y e^{-\beta y^2/2c_e}, \tag{4}$$

where v_0 is an arbitrary amplitude parameter, with dimensions of speed.

Solutions to $\hat{u}(y)$ and $\hat{Z}(y)$ are assumed to have the form

$$\hat{u}(y) = u^*(y)e^{-\beta y^2/2c_e}, \qquad \hat{Z}(y) = Z^*(y)e^{-\beta y^2/2c_e}. \tag{5}$$

The functions u^* and Z^* are then

$$u^*(y) = \frac{2iv_0\left(\frac{\beta}{c_e}\right)^{1/2}\left[\beta(\omega + kc_e)y^2 - kc_e^2\right]}{(\omega^2 - k^2c_e^2)}, \tag{6}$$

$$Z^*(y) = \frac{\omega}{gk}u^*(y) - \frac{2\beta i}{gk}v_0\left(\frac{\beta}{c_e}\right)^{1/2} y^2. \tag{7}$$

Note that, where the imaginary number $\pm i$ appears, it can be rewritten as $e^{\pm i\tau/4}$, with $\tau = 2\pi$. This can then be absorbed into the complex exponential in the full solution

to give $e^{i(kx-\omega t\pm\tau/4)}$, leading to a quarter-cycle shift to the east (west) in that part of the wave structure.

Rossby waves are low frequency, so the full dispersion relation can be approximated by neglecting the quadratic term in Equation (3) to get the approximate ($n = 1$) Rossby-wave dispersion relation,

$$\omega = -\frac{\beta k}{k^2 + 3\beta/c_e}. \tag{8}$$

Hence, for a given wavenumber k, the meridional wind v can be calculated from Equations (4) and (2). Using the frequency ω from Equation (8), the zonal wind u can then be calculated from Equations (6), (5), and (2). If desired, the geopotential height Z can be calculated from Equations (7), (5), and (2). The relative vorticity ζ and divergence D fields of the equatorial Rossby wave are then calculated as

$$\zeta = \frac{\partial v}{\partial x} - \frac{\partial u}{\partial y}, \qquad D = \frac{\partial u}{\partial x} + \frac{\partial v}{\partial y}. \tag{9}$$

The theoretical structure of a sample $n = 1$ equatorial Rossby wave is shown in Figure 1. This sample wave has a zonal wavenumber of 7 (i.e., seven complete wavelengths around the equator of an Earth-sized planet, such that $k = 1.10 \times 10^{-6}\,\mathrm{m}^{-1}$), and the gravity-wave speed was set to $c_e = 12\,\mathrm{m \cdot s^{-1}}$. These arbitrary values of the zonal wavenumber and gravity-wave speed were chosen so as to produce a sample theoretical equatorial Rossby wave with spatial characteristics approximating reasonably those of the observed CCERWs presented later in Section 3. From Equation (8), the (zonal) phase speed of this wave is $c_x = \omega/k = -3.30\,\mathrm{m \cdot s^{-1}}$. This wave pattern can be considered as representative of the lower tropospheric structure. When it is multiplied by the vertical structure calculated from the vertical structure equation, for example, the first internal mode (not shown), this leads to the same pattern but with opposite sign in the upper troposphere.

The wave structure has a pair of cyclonic vorticity anomalies, centred at 75°E, with westerlies on the Equator and easterlies off the Equator to the north and south. Equatorward flow to the west and poleward flow to the east completes the circulation around the cyclonic vorticity anomalies (anticlockwise in the Northern Hemisphere and clockwise in the Southern Hemisphere). The divergence field is symmetric about the Equator, with convergence to the east of the cyclonic anomalies and divergence to west. Convergence/divergence is actually a maximum off the Equator, at about 8° latitude for this example equatorial Rossby wave, with convergence in the poleward flow to the east and divergence in the equatorward flow to the west, mainly from the $\partial v/\partial y$ component. Hence, the initial expectation might be that the precipitation structure of the observed CCERWs (to be presented in Section 3.2) would follow the convergence structure of their theoretical

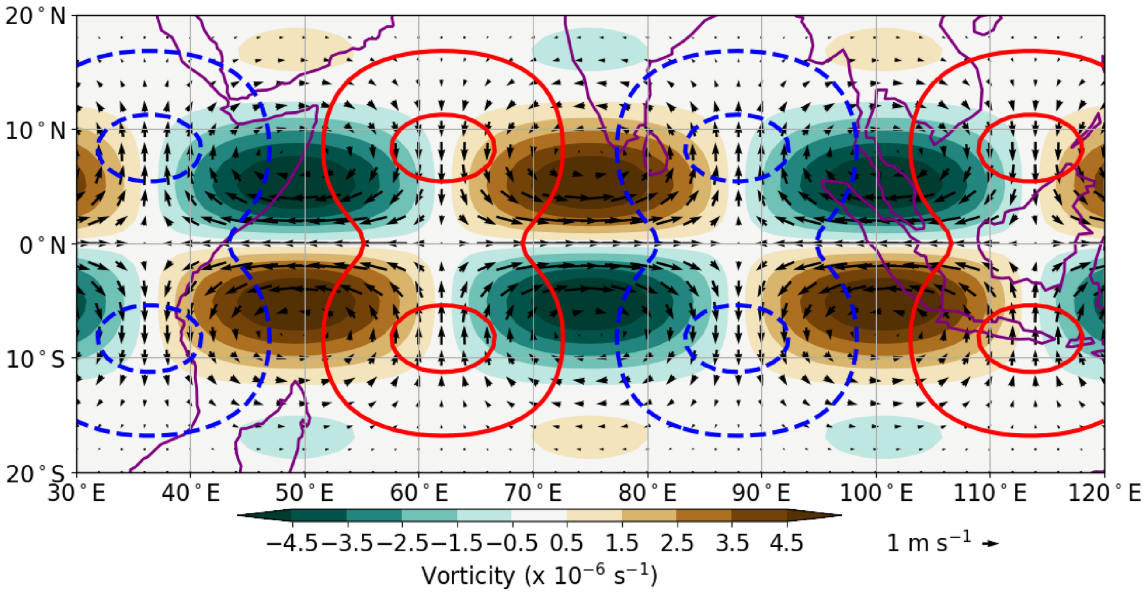

FIGURE 1 Structure of a sample theoretical linear equatorial Rossby wave with zonal wavenumber 7 ($k = 1.10 \times 10^{-6}\,\mathrm{m}^{-1}$), gravity-wave phase speed $c_e = 12\,\mathrm{m \cdot s^{-1}}$, and amplitude $v_0 = 1\,\mathrm{m \cdot s^{-1}}$. Horizontal wind vectors are shown by the black arrows (scale vector has length $1\,\mathrm{m \cdot s^{-1}}$). Relative vorticity is colour shaded, with interval $1 \times 10^{-6}\,\mathrm{s^{-1}}$; the first positive contour is at $0.5 \times 10^{-6}\,\mathrm{s^{-1}}$. Divergence is shown by the thick line contours with interval $0.3 \times 10^{-6}\,\mathrm{s^{-1}}$; positive contours are solid red and the first positive contour is at $0.15 \times 10^{-6}\,\mathrm{s^{-1}}$, while negative contours are blue dashed. Continental outlines are shown in purple for scale only.

counterpart and therefore be found to the east of the twin lower tropospheric cyclones and be approximately symmetric about the Equator, with off-equatorial maxima.

2.2 | Equatorial Rossby-wave vorticity budget

The vorticity equation for the flow on a single pressure (p) level can be written as

$$\frac{\partial \zeta}{\partial t} = \underbrace{-u\frac{\partial \zeta}{\partial x} - v\frac{\partial \zeta}{\partial y} - \omega\frac{\partial \zeta}{\partial p}}_{\text{advection of relative vorticity}} \quad \underbrace{-\zeta D - fD}_{\text{vortex stretching}} \quad \underbrace{-\beta v}_{\text{advection of planetary vorticity}} \quad \underbrace{-\left(\frac{\partial \omega}{\partial x}\frac{\partial v}{\partial p} - \frac{\partial \omega}{\partial y}\frac{\partial u}{\partial p}\right)}_{\text{tilting/twisting}}, \tag{10}$$

where ω is the vertical velocity in pressure coordinates. This leads to the concept of a vorticity budget, where the vorticity tendency $\partial\zeta/\partial t$ on the left is composed of the sum S of the vorticity source terms on the right. The vorticity budget for the theoretical equatorial Rossby wave is presented in Figure 2. In each panel, the vorticity field of the equatorial Rossby wave from Figure 1 is shown by the line contours, while the relevant vorticity source is colour-shaded.

The largest source term is advection of planetary vorticity $-\beta v$ (Figure 2a). Focusing on the Northern Hemisphere cyclone (positive vorticity anomaly) at 75°E, the equatorward flow to the west advects high planetary vorticity from the north, giving a positive vorticity tendency to the west. To the east, the poleward flow advects low planetary vorticity from the south, giving a negative vorticity tendency to the east. Hence, the vorticity source lies a quarter wavelength to the *west* of the vorticity anomaly and the net effect is to move the original cyclone (positive vorticity anomaly) westwards. This is the standard Rossby-wave propagation mechanism.

There is also a contribution from the $-fD$ vortex stretching term (Figure 2b). The convergence to the east of the cyclone (positive vorticity anomaly) leads to a positive vorticity tendency there. Similarly, the divergence to the west leads to a negative vorticity tendency. Hence, the $-fD$ vortex stretching source lies a quarter wavelength to the *east* of the vorticity anomaly, and its effect is one of eastward propagation. All the other vorticity source terms in Equation (10) are nonlinear and are zero for the linear theoretical equatorial Rossby wave.

The advection of planetary vorticity term is larger in magnitude than the vortex stretching term, hence the total source term (Figure 2c) has a positive vorticity tendency to the west of the cyclone (positive vorticity anomaly) and a negative vorticity tendency to the east. Therefore, the total source leads to the expected westward propagation of the equatorial Rossby wave.

Note that the theoretical budget presented here is not perfect. The vorticity tendency $\partial\zeta/\partial t$ (not shown) and the total vorticity source (Figure 2c) match each other very closely (their maps are visually indistinguishable). However, there is a small (2%) difference in amplitude. This arises from when the full dispersion relation (Equation 3) was approximated to the Rossby-wave dispersion relation (Equation 8).

The $-fD$ vortex stretching term effectively slows down the westward propagation speed of the equatorial Rossby wave. The westward tendency from the planetary vorticity advection term has a magnitude of approximately $28 \times 10^{-12}\,\mathrm{s}^{-2}$, but the (westward) total source term has a magnitude of only $21 \times 10^{-12}\,\mathrm{s}^{-2}$. Hence, if all other things were equal, the eastward tendency from the vortex stretching term would "slow down" the westward propagation speed of the wave by about 25%.

However, all other things are not equal, as the latitudinal structures of the $-\beta v$ and $-fD$ source terms (Figure 2a,b) are not the same and are not equal to the latitudinal structure of relative vorticity. However, when the two source terms are superimposed (Figure 2c), the total source term does have the same latitudinal structure as the relative vorticity. Hence, if the vortex stretching term was somehow removed, the remaining planetary vorticity advection term would not have the same latitudinal structure as the relative vorticity perturbation and the wave would *not* simply propagate westward with no change of shape.

Hence, any changes to the structure of observed CCERWs from the theoretical structure of equatorial Rossby waves will likely have impacts on the magnitude of the westward phase speed and also on the coherent structure of the wave.

3 | OBSERVED CONVECTIVELY COUPLED EQUATORIAL ROSSBY WAVE

In this section, the structure of observed CCERWs is revisited, focusing on their vorticity and divergence structures. A vorticity balance of observed CCERWs is constructed

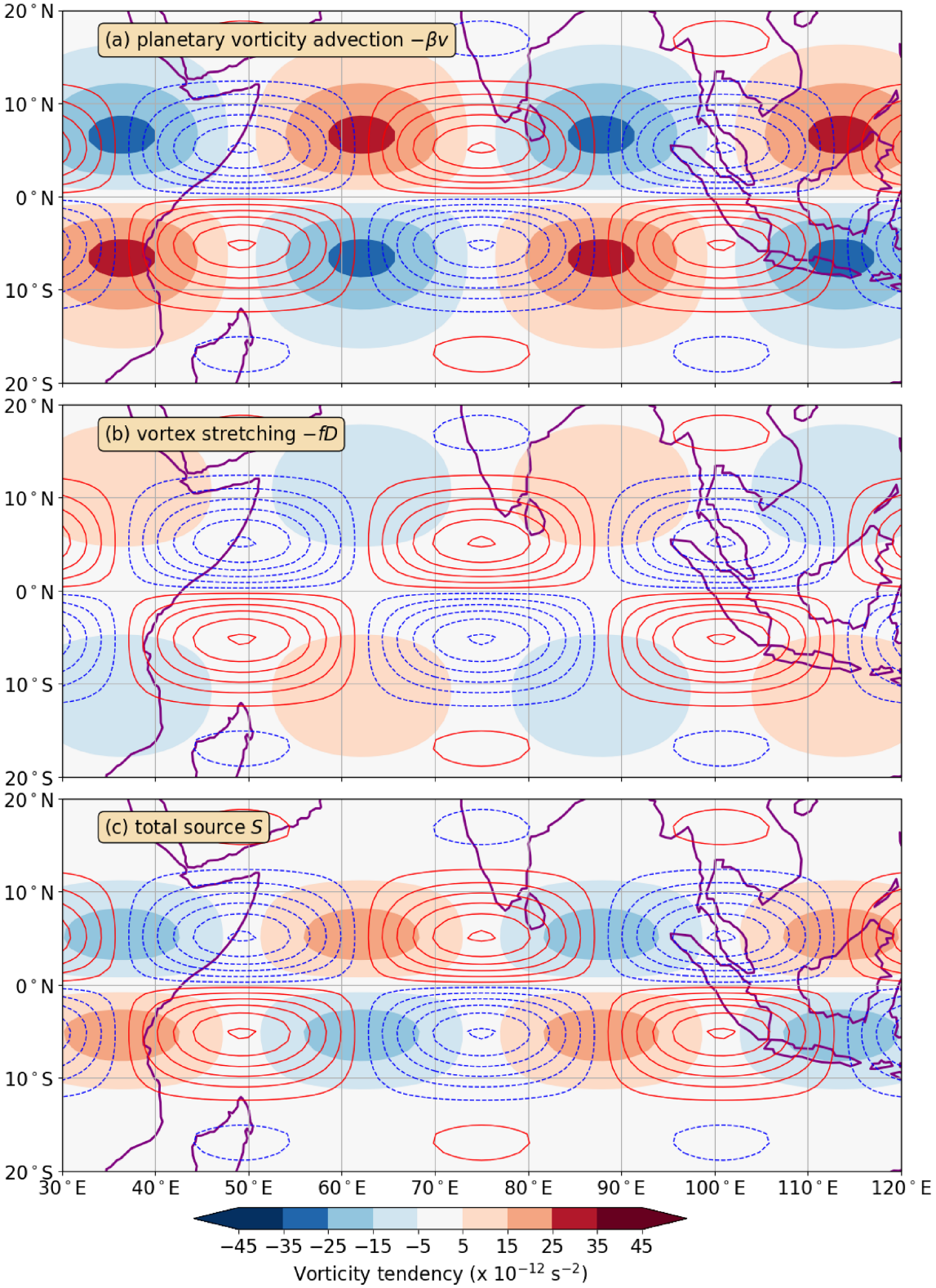

FIGURE 2 Vorticity source terms of the theoretical linear equatorial Rossby wave in Figure 1: (a) planetary vorticity advection $-\beta v$, (b) vortex stretching $-fD$, (c) total vorticity source (equal to vorticity tendency). Colour shading interval is 10×10^{-12} s^{-2}; the first positive level is at 5×10^{-12} s^{-2}. The vorticity anomaly is shown by line contours; the interval is 1×10^{-6} s^{-1}, positive contours are solid red with the first positive contour at 0.5×10^{-6} s^{-1}, and negative contours are dashed blue.

and compared with that of theoretical equatorial Rossby waves.

3.1 | Data and methodology

The dynamical structure and vorticity budget for CCKWs were previously analysed by Matthews (2021). Here, that methodology is adapted for CCERWs. Full details of the methodology are in Matthews (2021); an outline is provided here.

The CCERW analysis is based on the gridded Integrated Multi-satellitE Retrievals for GPM (IMERG) version 07B precipitation dataset (Huffman *et al.*, 2019). The IMERG data were retrieved from July 1, 2000–December 31, 2023, on a $0.1° \times 0.1°$ global latitude–longitude grid at 30-minute time resolution. They were regridded to a $0.25° \times 0.25°$ grid and three-hourly means for ease of computation.

The precipitation data were then latitudinally averaged from 15°S to 15°N, to effectively produce a Hovmöller time–longitude diagram of equatorial precipitation. Following Wheeler and Kiladis (1999), this Hovmöller diagram was then wavenumber–frequency filtered to extract the CCERW signals only; only westward-propagating waves lying between the dispersion curves of $n = 1$ equatorial Rossby waves with equivalent depths of 2.5 and 90 m, and with frequencies between 1/60 and 1/2.5 day^{-1} and zonal wavenumbers between 1 and 10, were passed by the filter. Following Baranowski *et al.* (2016), CCERW trajectories were then defined to lie along the maxima in this Hovmöller diagram of CCERW wavenumber–frequency filtered precipitation. This leads to a full pantropical event-based dataset of CCERW trajectories.

A base point was then defined at 75°E in the central Indian Ocean for this study. A total of 208 CCERW trajectories crossed this base point during their lifetimes, producing a set of 208 crossing times. Lagged composite means were constructed by averaging any variable of interest over those 208 crossing times. Hence, lag day 0 corresponds to the time of the CCERW crossing the base point at 75°E. Composites of the IMERGV07B precipitation itself were constructed initially, to identify the convective/precipitation signal associated with CCERWs.

For dynamical variables (zonal and meridional wind components, horizontal divergence, relative vorticity), the ERA5 reanalysis dataset was used (Hersbach *et al.*, 2020). The ERA5 data were initially on a $0.25° \times 0.25°$ grid with hourly time resolution. These were regridded to an approximately $0.7° \times 0.7°$ grid and three-hourly means for ease of computation. Prior to compositing, the ERA5 data were also wavenumber–frequency filtered (separately at each latitude) for CCERW signals to increase the signal-to-noise ratio.

3.2 | CCERW precipitation and dynamical structure

The lagged composites of precipitation anomaly for the base point at 75°E in the Indian Ocean (Figure 3) show the westward propagation of the CCERW. At lag −3 days (i.e., three days before the CCERWs cross the base point at 75°E), there are positive precipitation anomalies in the sector from 70–100°E (Figure 3a). These are approximately symmetric about the Equator, with off-equatorial maxima. This indeed appears to be similar to the spatial structure suggested by the lower-tropospheric convergence anomalies in the theoretical equatorial Rossby wave (Figure 1) described in Section 2.1. At lag 0 days, the precipitation anomalies have moved westward, to be centred at the base point at 75°E, by design (Figure 3b). The equatorial precipitation anomalies have weakened, so that the structure is now mainly composed of two off-equatorial maxima. At lag 3 days, the precipitation anomalies have moved further westward, to around 65°E (Figure 3c). The weak positive precipitation anomalies on the Equator between these two off-equatorial maxima have now disappeared and been replaced by negative precipitation anomalies. Additionally, a developing larger scale region of negative precipitation anomalies from approximately 12°S–12°N has strengthened and also moved westward, behind (i.e., to the east of) the positive precipitation anomalies.

Note that these lagged composites of precipitation have been calculated from *unfiltered* precipitation anomalies. The mean annual cycle was calculated and subtracted, but no wavenumber–frequency filtering was performed. The magnitudes of these unfiltered composite precipitation anomalies are up to 5 mm· day^{-1}, which is approximately 50% of the value of the mean precipitation signal in this region. Hence, these CCERW precipitation anomalies constitute a very strong, robust signal.

The dynamical structure of the CCERWs is investigated through lagged composites of lower tropospheric (850 hPa) dynamical variables (Figure 4), for comparison with the dynamical structure of theoretical equatorial Rossby waves (Figure 1) and as a prelude to the calculation of the CCERW vorticity budget. At lag −3 days (Figure 4a), the convergence field (blue dotted line contours) matches well the regions of positive precipitation anomalies in Figure 3a, with an approximately equatorially symmetric band of convergence in the sector from 70–100°E, with slightly weaker convergence on the Equator and off-equatorial maxima in convergence off the

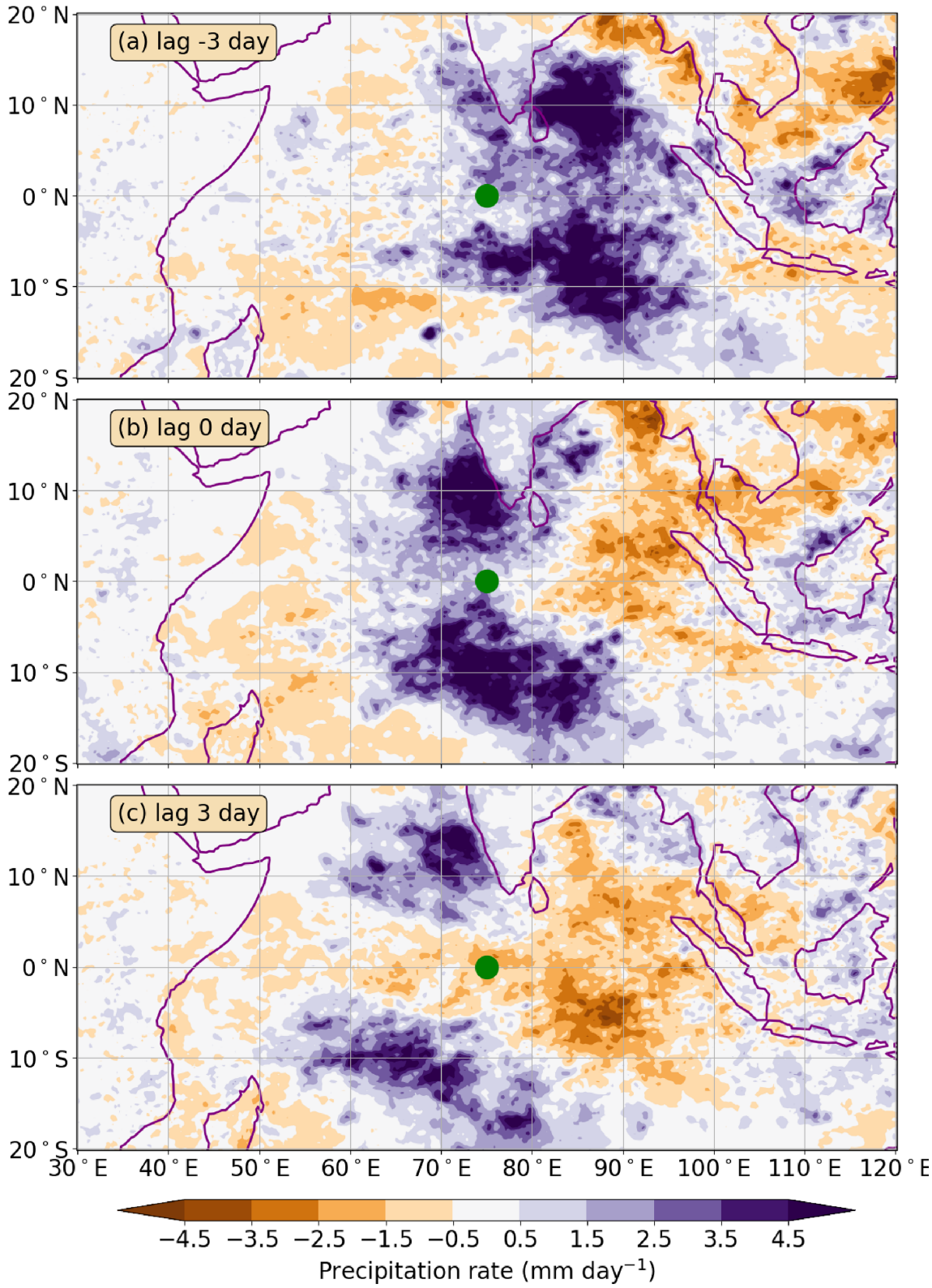

FIGURE 3 Lagged composite maps of precipitation anomalies for CCERW over the Indian Ocean at lags (a) −3, (b) 0, and (c) 3 days. The precipitation contour interval is 1 mm · day^{-1}. The base point at 75°E is shown by the green filled circle.

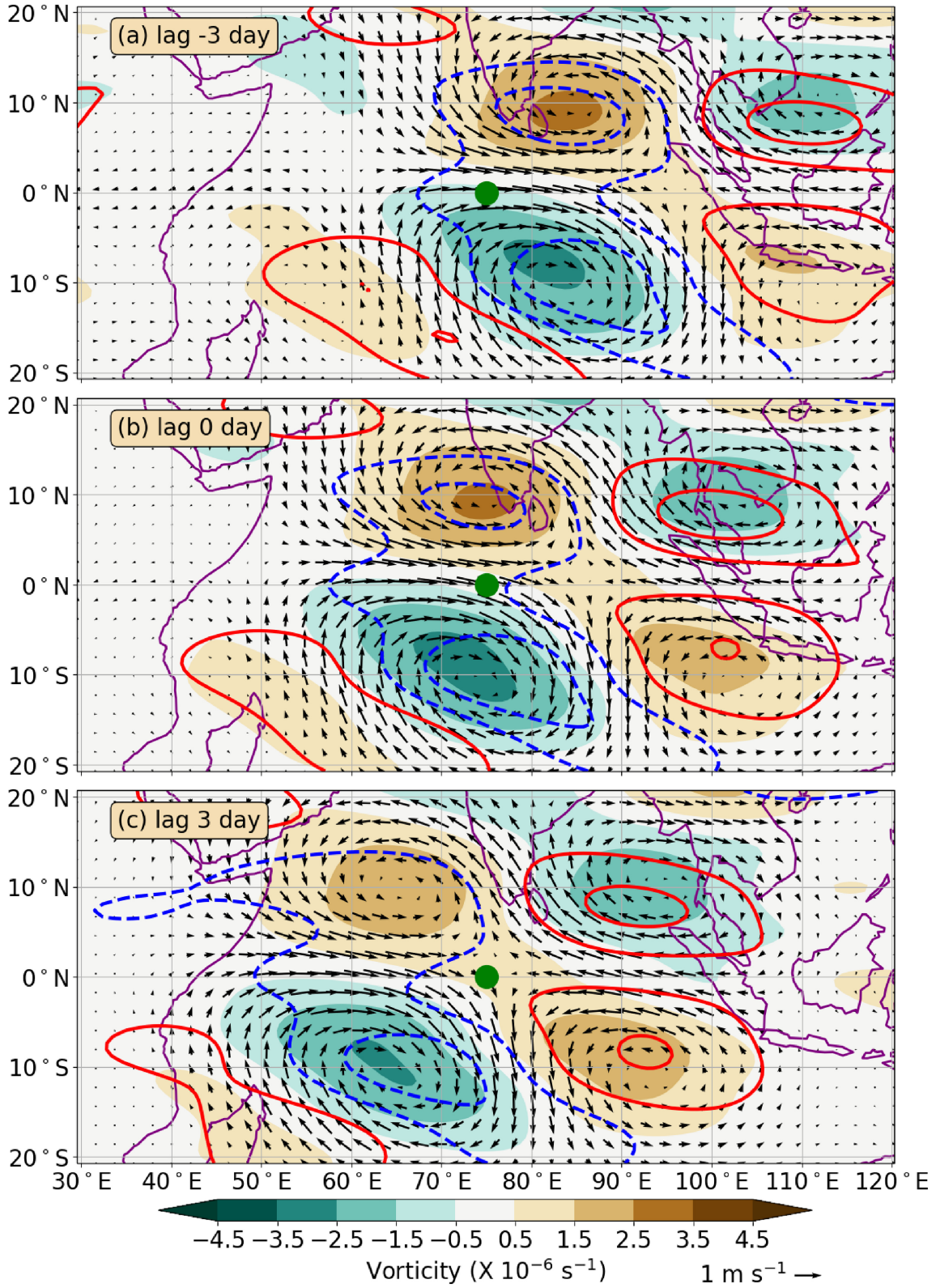

FIGURE 4 Lagged composite maps of dynamical anomalies of CCERW at 850 hPa, for days (a) −3, (b) 0, and (c) +3. Horizontal wind vectors are shown by the black arrows (scale vector has length 1 m · s^{-1}). Relative vorticity is colour shaded, with interval 1×10^{-6} s^{-1}; the first positive contour is at 0.5×10^{-6} s^{-1}. Divergence is shown by line contours with interval 0.25×10^{-6} s^{-1}; positive contours are solid red with the first positive contour at 0.125×10^{-6} s^{-1}, and negative contours are dashed blue. The dynamical fields were wavenumber–frequency filtered for CCERW signals before compositing.

Equator around 8° latitude in both hemispheres. This latitudinal structure of the convergence anomalies in the CCERW bears a strong resemblance to the corresponding convergence anomalies in the theoretical equatorial Rossby wave (Figure 1).

The wind and vorticity anomalies in the CCERW also bear a strong similarity to the theoretical wave, with two off-equatorial cyclonic vorticity anomalies with westerly anomalous flow on the Equator in between them. However, we recall that in the theoretical equatorial Rossby wave (Figure 1) the convergence anomalies lay a quarter cycle to the *east* of the cyclone pair. In the CCERW (Figure 4a), the convergence anomalies are *coincident* (in phase) with the cyclone pair. Given the role of the convergence/divergence anomalies in retarding the westward propagation of the theoretical equatorial Rossby wave, this change in phase relationship will almost certainly have an impact on the propagation and possibly growth mechanisms in the CCERW.

By lag 0 days, the lower tropospheric cyclone pair and accompanying convergence (Figure 4b) and enhanced precipitation anomalies (Figure 3b) have moved westward to the base point at 75°E. By lag 3 days, the whole dynamical structure has moved further westward to 65°E. Within each of the lower tropospheric off-equatorial cyclonic anomalies, there is still convergence (Figure 4c) and enhanced precipitation (Figure 3c). However, on the Equator the precipitation appears to have become decoupled from the dynamical structure, with reduced precipitation coincident with lower tropospheric convergence.

The change in structure in the vertical can be seen from the zero-lagged dynamical CCERW composites at selected levels: the boundary layer (975 hPa; Figure 5d); the free lower troposphere (850 hPa; Figure 5c); the middle troposphere (500 hPa; Figure 5b); and the upper troposphere (200 hPa; Figure 5a). Overall, there is very little vertical tilt in the lower to middle troposphere, with the wind and vorticity structures stacking up at each level (Figure 5b–d). This is consistent with previous studies of CCERWs (Inoue *et al.*, 2020; Nakamura & Takayabu, 2022b) and is in contrast to the structure of the gravity-type modes (CCKWs, convectively coupled mixed Rossby–gravity waves and eastward inertio-gravity waves), which show a pronounced upward tilt to the west, against their direction of propagation (Kiladis *et al.*, 2009; Matthews, 2021; Wheeler *et al.*, 2000).

Although the convergence regions in the CCERWs do remain co-located with the cyclonic vorticity anomalies throughout the lower to middle troposphere, their horizontal spatial structure does change with height. In the boundary layer at 975 hPa, the convergence is strong and almost entirely within the off-equatorial cyclonic vorticity anomalies (Figure 5d). In the free lower troposphere at 850 hPa, as previously noted, the convergence is still strongest within the off-equatorial cyclonic vorticity anomalies, but there is also significant convergence along the Equator (Figure 5c). By the middle troposphere at 500 hPa, the strongest convergence is actually at the Equator, with weaker convergence within the off-equatorial cyclonic vorticity anomalies (Figure 5b). At all levels in the lower to middle troposphere, the CCERW structure does resemble a modified theoretical equatorial Rossby wave.

However, the structure in the upper troposphere at 200 hPa is rather different (Figure 5a). The expected structure, assuming a first internal mode vertical structure, is of a similar spatial pattern to the lower troposphere, but with a sign reversal. There is some evidence for this type of structure in the composite CCERW; at the longitude of the base point (75°E) there is upper tropospheric divergence with off-equatorial maxima above the lower tropospheric convergence. There is also a (weak) anticyclonic vorticity pair (negative in Northern Hemisphere, positive in Southern Hemisphere) above the cyclonic vorticity pair in the lower troposphere. However, the vector wind field is different, and is dominated by a large-scale divergent outflow both polewards (a local Hadley circulation) and eastwards (a local Walker circulation). This is a major departure from the expected theoretical structure. Similar behaviour was also observed in the upper tropospheric structure of CCKWs (Matthews, 2021). Hence, it appears that, apart from the horizontal phase relationship between vorticity and divergence, convectively coupled equatorial waves in general bear some resemblance to their theoretical counterparts in the lower troposphere, but have a radically different, divergent outflow structure in the upper troposphere.

3.3 | CCERW vorticity budget

Given that the 850-hPa free lower tropospheric structure of the CCERW is fairly representative of the structure throughout the lower and middle troposphere, a vorticity budget of the CCERW is carried out at this level to ascertain the dynamical propagation and growth mechanisms. The seven individual vorticity source terms are shown in Figure 6a–g. These have been spatially smoothed using triangular truncation in spectral space at total wavenumber 42 (Dawson, 2016).

The planetary vorticity advection ($-\beta v$) term (Figure 6f) in the CCERW has positive tendencies (colour shading) to the west of positive vorticity anomalies (line contours) and negative tendencies to the east. Hence, this Rossby-wave propagation mechanism still contributes strongly to westward propagation of the CCERW, just as it

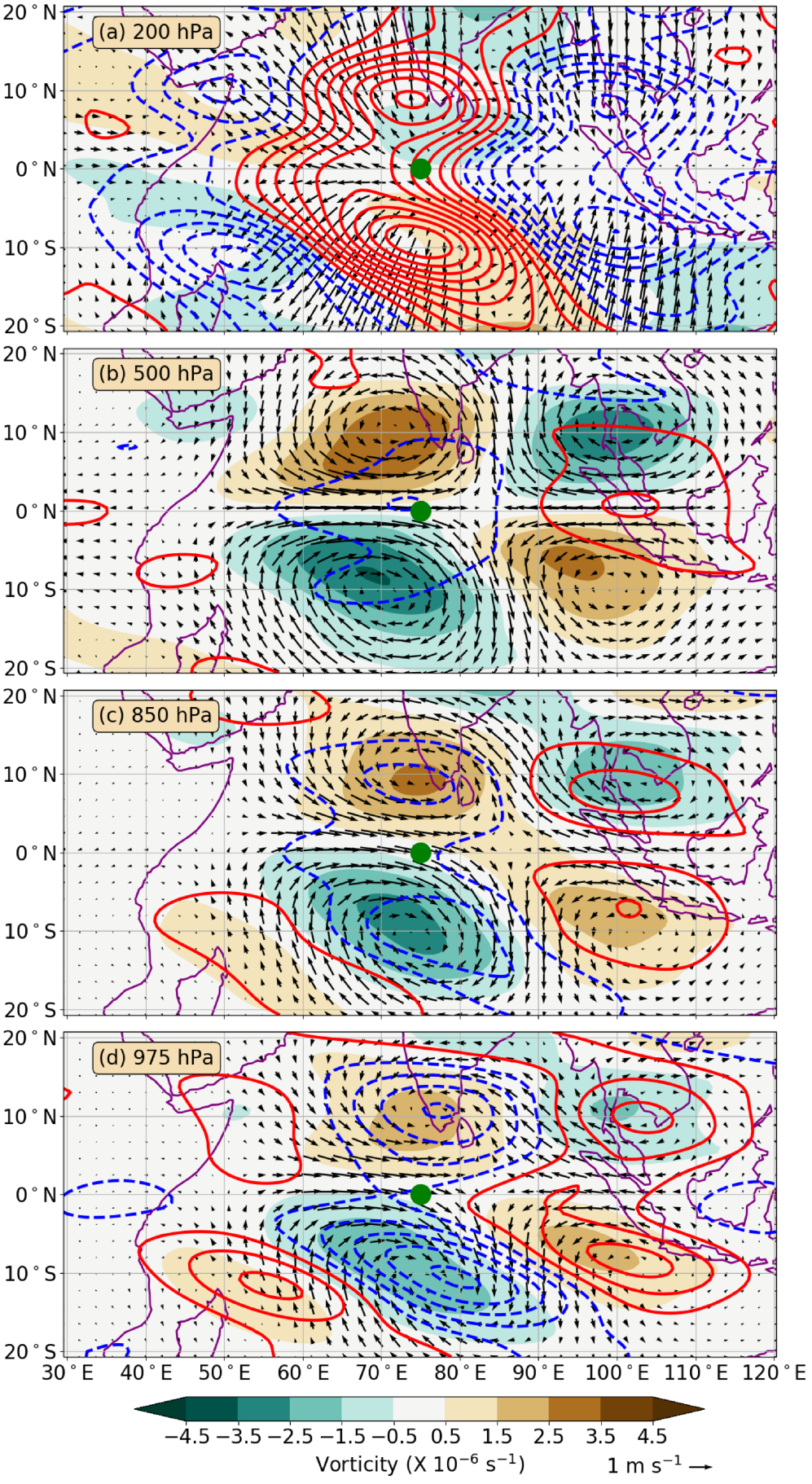

FIGURE 5 Zero-lagged composite maps of dynamical anomalies of CCERW at (a) 200, (b) 500, (c) 850, and (d) 975 hPa. Conventions as in Figure 4.

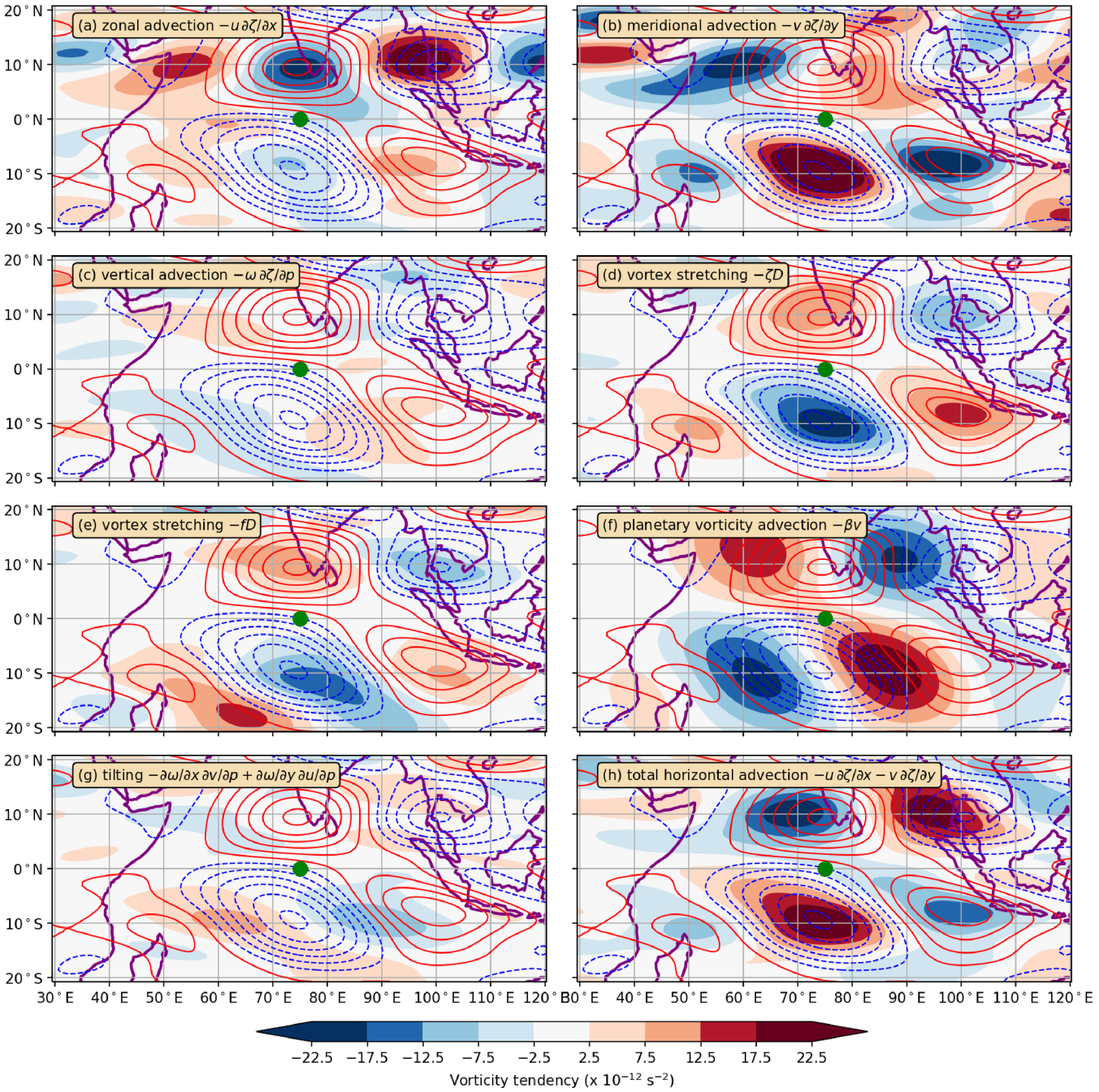

FIGURE 6 Zero-lagged composite maps of individual source terms in vorticity budget of CCERW at 850 hPa: (a) zonal advection $-u\partial\zeta/\partial x$, (b) meridional advection $-v\partial\zeta/\partial y$, (c) vertical advection $-\omega\partial\zeta/\partial p$, (d) vortex stretching $-\zeta D$, (e) vortex stretching $-fD$, (f) planetary vorticity advection $-\beta v$, (g) tilting $-\partial\omega/\partial x\,\partial v/\partial p + \partial\omega/\partial y\,\partial u/\partial p$, (h) total horizontal advection $-u\partial\zeta/\partial x - v\partial\zeta/\partial y$. Colour shading interval is 5×10^{-12} s^{-2}; the first positive level is at 2.5×10^{-12} s^{-2}. The vorticity anomaly is shown by line contours; the interval is 0.5×10^{-6} s^{-1}, positive contours are solid red and the first positive contour is at 0.25×10^{-6} s^{-1}, and negative contours are dashed blue.

does in the theoretical equatorial Rossby wave (Figure 2a). It would be difficult to conceive of a situation where this was not the case, as a cyclonic anomaly has, almost by definition, equatorward flow to the west, which will then advect high-value (cyclonic) potential vorticity to the west, leading to westward propagation.

The only other non-zero vorticity source term in the theoretical equatorial Rossby wave was the vortex stretching ($-fD$) term (Figure 2b). As discussed in Section 2.2, the quarter-cycle phase difference between the vorticity and divergence fields led to a (weak) eastward propagation tendency. However, in the CCERW, the convergence anomaly

is in phase with the cyclonic vorticity, leading to *growth* rather than propagation (positive tendency in phase with the positive vorticity in Figure 6 e).

If the CCERW behaved like the theoretical equatorial Rossby wave, then the remaining five vorticity source terms (Figure 6a–d,g) would be zero. This is clearly not the case. The other vortex stretching term ($-\zeta D$; Figure 6d), from the nonlinear interaction between relative vorticity and divergence, also has positive vorticity tendencies in phase with positive vorticity anomalies. Hence, this term also leads to growth.

There are also strong contributions from the two horizontal advection terms. The zonal advection ($-u\partial\zeta/\partial x$; Figure 6a) term has quite a complex spatial structure. It is strongest in the Northern Hemisphere, with a large negative tendency at the location of the positive vorticity anomaly at 75°E, 10°N and a large positive tendency at the location of the negative vorticity anomaly at 100°E, 10°N. These vorticity tendencies will interfere destructively with the vorticity pattern, leading to *decay* of the CCERW. The situation in the Southern Hemisphere is opposite, with, for example, a negative tendency at the location of the negative vorticity anomaly at 75°E, 10°S, leading to growth. However, the anomalies in the Southern Hemisphere are considerably weaker, and the overall behaviour will likely be dominated by the Northern Hemisphere structure.

The meridional advection ($-v\partial\zeta/\partial y$; Figure 6b) term also has a complex spatial structure. This is strongest in the Southern Hemisphere where the tendency and vorticity anomalies are out of phase, leading to decay. However, in the Northern Hemisphere the positive tendency at 85°E, 10°N is to the east of the positive vorticity anomaly at 75°E, 10°N, leading to an eastward propagation tendency. The total horizontal advection term (Figure 6h; the sum of panels a and b) shows more clearly the net effect of horizontal advection, which is to interfere destructively with the vorticity pattern, leading to decay. The vertical advection (Figure 6c) and the tilting/twisting term (Figure 6g) are both weak and will contribute little to propagation or growth.

The propagation and growth characteristics of each vorticity source term are quantified in a polar propagation–growth diagram (Figure 7). The methodology is described in full detail in Matthews (2021). To summarise, a domain of interest is first defined, centred on the base point at 75°E and the Equator (55–95°E, 18°S–18°N). For a particular vorticity source term of interest, the root-mean-square (RMS) amplitude of that vorticity source term over the domain is calculated and then normalised by the RMS amplitude of the vorticity tendency ($\partial\zeta/\partial t$) term. Then, cosine waves in the zonal direction are fitted to the vorticity anomaly and the vorticity source term over the domain. The phase difference between the vorticity field and the vorticity source term is then the phase difference between these two cosine waves; this is expressed as a multiple of τ (radians), where $\tau = 2\pi \approx 6.283\ldots$ radians is equivalent to one full turn (Abbott, 2012).[1] These two quantities (normalised RMS amplitude, phase difference) are plotted as a point on the polar propagation–growth diagram (Figure 7).

By construction, the point for the vorticity tendency $\partial\zeta/\partial t$ term lies very close to the position $(1.00, -0.25\tau)$, as its normalised amplitude (normalised by itself) is 1, and the vorticity tendency (of a propagating wave) is a quarter cycle out of phase with the vorticity. The diagram is oriented so that a phase difference of -0.25τ (leading by a quarter cycle) is on the left side of the diagram, indicating westward propagation; a phase difference of 0.25τ (lagging by a quarter cycle) is on the right side, indicating eastward propagation; a phase difference of 0 (in phase) is at the top, indicating growth; and a phase difference of 0.5τ (out of phase) is at the bottom, indicating decay.

The planetary vorticity advection $-\beta v$ term has large amplitude and is in the blue westward-propagating quadrant, indicating that it is the term that contributes most strongly to the westward propagation of the CCERW. Both vortex stretching terms ($-fD$ and $-\zeta D$) are in the red growth quadrant, and vortex stretching is evidently the process by which the CCERW grows. The horizontal advection terms both lie in the red decay quadrant, with the meridional advection term also contributing to a slight eastward propagation tendency. The total horizontal advection term (sum of zonal and meridional advection) lies between these two, as expected, in the decay quadrant. The remaining terms (vertical advection and tilting/twisting) lie near the centre of the diagram, as their amplitudes are weak. They do not contribute significantly to the vorticity budget.

The total source term S, shown by the purple marker, lies in the westward-propagating quadrant, but also on the edge of the growth quadrant, thus the net effect of all the source terms is one of westward propagation and growth. The residual term ϵ (yellow marker in Figure 7) is calculated as the difference between the vorticity tendency $\partial\zeta/\partial t$ and total source S terms. It represents subgrid-scale terms that are not calculated explicitly by the other vorticity source terms, plus any numerical errors in the calculation of the individual source terms due to discretisation (gridding) of the data. As subgrid-scale terms tend to be generally diffusive, it is not surprising that this term lies in the decay quadrant. The magnitude of the residual term (distance from the centre of the polar plot) is larger than those of the vertical advection and tilting terms, similar to those of the vortex stretching and horizontal advection terms, and smaller than the dominant advection of planetary vorticity term. Hence, subgrid-scale processes/

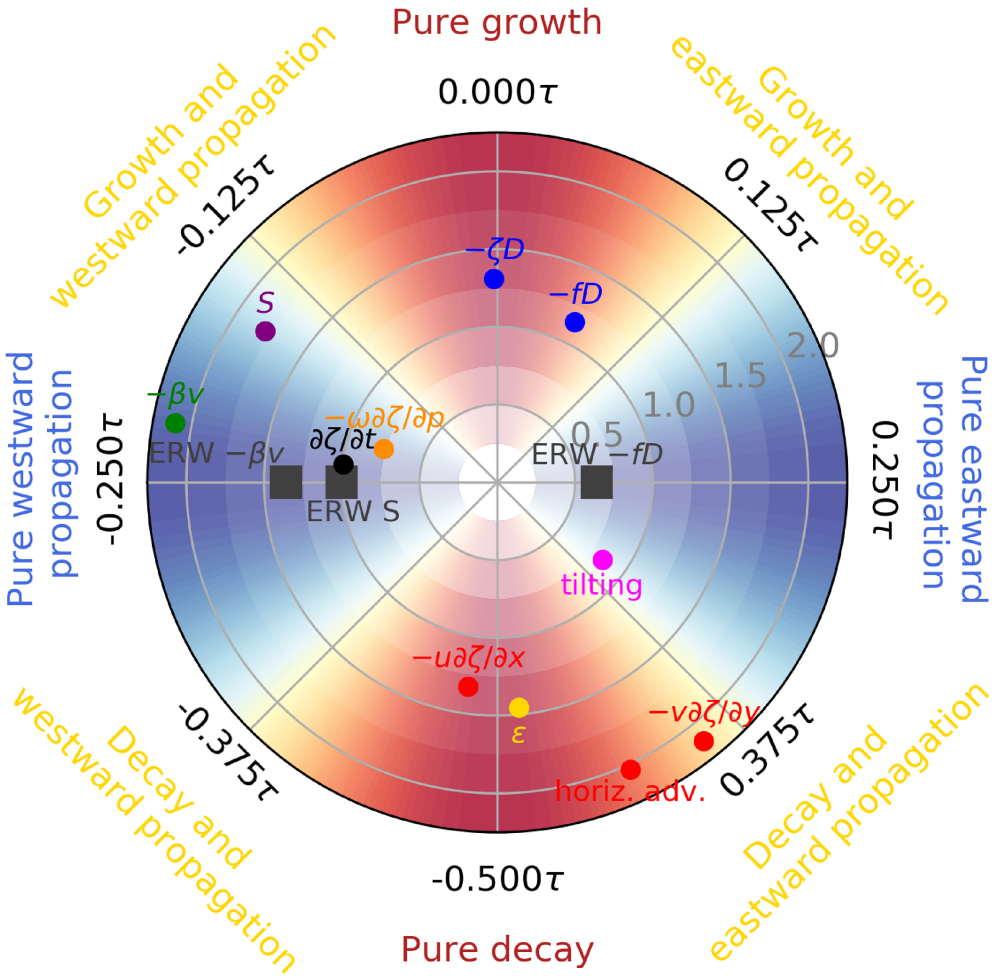

FIGURE 7 Vorticity budget propagation–growth polar diagram of 850-hPa CCERW vorticity source terms, with normalised RMS amplitude as the radial coordinate and phase difference θ between the source term and the vorticity anomaly as the azimuthal coordinate. Contrary to regular convention, the azimuthal coordinate axis is zero on the positive vertical axis and increases in a clockwise direction. This enables growth to be toward the top of the diagram, decay to the bottom, westward propagation to the left, and eastward propagation to the right. The two individual source terms ($-\beta v$ and $-fD$) and the total source term (S) for a theoretical equatorial Rossby wave are shown by the large grey squares.

numerical errors certainly contribute to the overall vorticity budget.

Finally, for comparison, the vorticity-budget terms from the theoretical equatorial Rossby wave are shown by square markers in Figure 7. These lie on the pure propagation line in the diagram, with the planetary vorticity advection $-\beta v$ term contributing strongly to westward propagation and the vortex stretching $-fD$ term contributing weakly to eastward propagation. The total source S terms lies at the point $(1.00, -0.25\tau)$, corresponding to pure westward propagation with no growth.

4 | CONCLUSIONS

The dynamical mechanisms of propagation and growth in observed CCERWs were analysed via a vorticity budget of ERA5 reanalysis data using a database of CCERW events calculated from IMERG precipitation. This was compared with a vorticity budget of theoretical equatorial Rossby waves, under the hypothesis that CCERWs would act dynamically like modified versions of those theoretical waves.

As anticipated, the main mechanism for westward propagation of CCERWs is through advection of planetary vorticity (the $-\beta v$ term), that is, the standard Rossby-wave propagation mechanism. Equatorward flow to the west of the off-equatorial cyclonic anomalies advects high-magnitude (cyclonic) planetary vorticity into the region west of the original cyclonic anomaly. Poleward flow to the east of the off-equatorial cyclonic anomalies advects low-magnitude (anticyclonic) planetary vorticity into the region east of the original cyclonic anomaly and west of the trailing anticyclonic anomaly. The net result is a westward propagation of the vorticity pattern.

In the theoretical equatorial Rossby wave, linear vortex stretching (the $-fD$ term) gives a weak eastward propagation tendency. The convergence in the theoretical wave lies to the east of the off-equatorial cyclonic anomalies, from negative $\partial u/\partial x$ on the Equator and negative $\partial v/\partial y$ off the Equator. This leads to vortex stretching and a cyclonic vorticity tendency to the east of the cyclonic vorticity anomalies, and hence an eastward propagation tendency. This acts effectively to slow the westward phase speed of the theoretical wave from its non-divergent equivalent.

However, this mechanism is very different in CCERWs. In the lower troposphere, convergence is in phase with the off-equatorial cyclonic anomalies. The resulting cyclonic vorticity tendency from vortex stretching at the same location as the cyclonic vorticity anomalies leads to growth of the CCERW. Both the linear ($-fD$) and nonlinear ($-\zeta D$) vortex stretching terms contribute to this growth. This change in the role of vortex stretching, from a weak eastward propagation tendency in the theoretical wave to growth in the CCERW, will lead to an effective increase in the actual westward propagation speed of the CCERW, by up to 25%. The horizontal vorticity advection and the subgrid-scale terms also have important roles and act to dampen the CCERW. The total vorticity source for CCERWs is one of both westward propagation and slight growth. This contrasts with the total vorticity source for theoretical equatorial Rossby waves, which is one of pure westward propagation.

In the upper troposphere, the CCERW structure is quite different and is dominated by a large-scale divergent outflow, rather than an equatorial Rossby-wave-like structure. This is perhaps not surprising when the background flow in the region is considered. Over the Indian Ocean, the background flow in the lower troposphere is typically a weak westerly, while in the upper troposphere it is a strong easterly, with a resulting vertical shear of up to $20\,\mathrm{m}\cdot\,\mathrm{s}^{-1}$ over the depth of the troposphere. This will act to shear out any vertical modal structure present, and one of the major, limiting assumptions in the traditional, theoretical, linear equatorial wave analysis is that the background flow is zero (and therefore has zero vertical shear). In reality, it appears that the CCERW structure is set by equatorial Rossby-wave dynamics interacting with convection in the lower troposphere, with a divergent outflow structure aloft.

These results have implications for modelling of CCERWs and prediction of CCERW-related precipitation and wind fields in climate modelling and numerical weather forecasting frameworks. Models need to simulate the internal structure of CCERWs correctly, especially the phase relationships between vorticity and divergence, to simulate growth rates and propagation speeds correctly. Errors in growth rates will lead to incorrect predictions of the strength of a CCERW system, and errors in propagation speed will lead to incorrect predictions of the timing of arrival of CCERW-related weather phenomena (e.g., extreme precipitation, winds). The CCERW event and vorticity-budget diagnostics presented here can also be applied to numerical weather prediction (NWP) data to assess model fidelity in simulating these CCERW processes.

CCERWs and other equatorial wave structures can now be readily identified in real-time data and this information used to inform real-time forecasts (Yang *et al.*, 2021). Indeed, the importance of simulating the dynamical structures of CCERWs correctly has been highlighted recently (Ferrett *et al.*, 2023), even if the model concerned has less skill in predicting the precipitation structures associated with CCERWs. Here, the ability of a forecast model to predict the dynamical development of CCERWs skilfully was combined with the known observed relationship between extreme precipitation and the CCERW dynamical structure, to produce hybrid dynamical–statistical forecasts of CCERW-related extreme precipitation. The skill of this hybrid model exceeds the skill of the actual NWP simulated precipitation (i.e., the direct precipitation forecast) over the South Philippines and in central Vietnam. This system is still in its relative infancy, but has high potential for the future of predicting CCERW-associated extreme precipitation.

This study investigated the *dynamical* mechanisms behind propagation and growth in a CCERW, using a vorticity budget. It is therefore only a partial analysis of the driving mechanisms behind CCERWs. Of course the mechanism behind the coupling of convection and the dynamics is also crucial and, one could argue, more fundamental.

CCERW convection is observed to be in phase with the total column water anomaly, and convection in the active region of CCERWs is actually due to mesoscale convective systems being triggered there (Nakamura & Takayabu, 2022a). The existence of the total column water anomaly is likely to be due to (moisture) convergence. The moist convection then leads to large-scale ascent and spin-up of vorticity through vortex stretching ($-fD$ and $-\zeta D$ terms). Hence, cyclonic vorticity in the CCERW is in phase with lower tropospheric convergence. As seen from the vorticity-budget analysis presented here, this in-phase relationship is crucial for the growth of CCERWs, and also the CCERW propagation speed, as it removes the eastward retarding tendency of the $-fD$ term that exists in dry theoretical waves, effectively speeding up the coupled wave in comparison with its theoretical counterpart.

Theoretical and numerical analyses using the moisture mode and WISHE frameworks have also established the link between theoretical equatorial Rossby waves and CCERW-type structures. Fuchs-Stone *et al.* (2019) found that the equatorial Rossby wave in a dry atmosphere transitioned to a westward-propagating WISHE–moisture mode (CCERW analogue) when convection was switched on. The westward propagation speed of the wave decreased when convective coupling was allowed, mainly due to WISHE and cloud–radiation interactions. A thermodynamic instability was found, from interactions between surface fluxes and atmospheric moisture. Further analysis within the WISHE framework found that a background

easterly flow and pre-moistening by WISHE contributed to the westward propagation of the mode, and that growth occurred through destabilisation by WISHE and the background easterly shear (Chen, 2022).

Several lines for future work present themselves. The dynamical analysis presented here through the vorticity budgets and the previous thermodynamical analyses using the WISHE and moisture mode frameworks should be self-consistent and a combined analysis of CCERWs using both these approaches is desirable. Also, there is an interesting question of how and why the transition in structure (in particular the phasing between vorticity and divergence) between an idealised dry equatorial Rossby wave and a fully fledged moist CCERW comes about, as processes such as boundary-layer friction and the strength of the convective coupling are increased.

The focus in this study was on the Indian Ocean, as its large ocean basin with fairly homogeneous sea-surface temperature distributions was considered likely to lead to the simplest and most generally applicable analysis of the CCERW dynamical structures. It is an open question whether the same relationships will hold in the other regions of the Tropics. How will the complex island geometry of the Maritime Continent affect the CCERW structures? Will the warm sea-surface temperatures and narrow ITCZs north of the Equator in the Pacific and Atlantic basins have a major effect? How will land–atmosphere interactions over Africa and South America affect the CCERW phase relationships documented here?

This vorticity-budget approach has been applied to CCKWs (Matthews, 2021) and in this study to CCERWs. Other convectively coupled equatorial waves, such as mixed Rossby–gravity waves, should also be amenable to this type of analysis. Indeed, vorticity diagnostics of convectively coupled mixed Rossby–gravity waves have already been shown to be useful in analysing their role in the generation of African easterly waves (Yang *et al.*, 2018).

In summary, a vorticity-budget framework has been presented for CCERWs to explain their propagation and growth characteristics, from a dynamical-only perspective, over the Indian Ocean. This approach appears to have potential in diagnosing climate and NWP model errors, and in a wider thermodynamical–dynamical analysis of convectively coupled equatorial waves.

ACKNOWLEDGEMENTS

The research presented in this article was carried out on the High Performance Computing Cluster supported by the Research Computing Service at the University of East Anglia. I was partially supported by the Natural Environment Research Council through the Terra-Maris project (grant NE/R016704/1). I thank the three anonymous reviewers, whose comments helped to improve the article.

DATA AVAILABILITY STATEMENT

All data used in this analysis are publicly available. The IMERG precipitation data were supplied by the National Aeronautics and Space Administration through their web site at gpm.nasa.gov. ERA-5 data were accessed from Copernicus at https://cds.climate.copernicus.eu (doi: 10.24381/cds/bd0915c6). The Python code used for the analysis is archived at https://github.com/adrianjmatthews/py36/.

ENDNOTE

[1]Hence, for example, a quarter cycle is written as the more natural $\tau/4$ radians, rather than the unintuitive $\pi/2$ radians.

ORCID

Adrian J. Matthews https://orcid.org/0000-0003-0492-1168

REFERENCES

Abbott, S. (2012) My conversion to Tauism. *Math Horizons*, 19, 34.

Baranowski, D.B., Flatau, M.K., Flatau, P.J., Karnawati, D., Barabasz, K., Labuz, M. et al. (2020) Social-media and newspaper reports reveal large-scale meteorological drivers of floods on Sumatra. *Nature Communications*, 11, 2503.

Baranowski, D.B., Flatau, M.K., Flatau, P.J. & Matthews, A.J. (2016) Impact of atmospheric convectively-coupled Kelvin waves on upper ocean variability. *Journal of Geophysical Research*, 121, 2045–2059.

Chen, G. (2022) A model of the convectively coupled equatorial Rossby wave over the Indo-Pacific warm pool. *Journal of the Atmospheric Sciences*, 79, 2267–2283.

Dawson, A. (2016) Windspharm: A high-level library for global wind field computations using spherical harmonics. *Journal of Open Research Software*, 4, e31.

Dias, J., Gehne, M., Kiladis, G.N. & Magnusson, L. (2023) The role of convectively coupled equatorial waves in sub-seasonal predictions. *Geophysical Research Letters*, 21, e2023GL106198.

Diong, J.Y., Xavier, P., Woolnough, S.J. & Abdullah, F.A. (2023) Equatorial Rossby waves on cold surge days and their impact on rainfall. *Quarterly Journal of the Royal Meteorological Society*, 149, 2031–2047.

Feng, X., Yang, G.Y., Hodges, K.I. & Methven, J. (2023) Equatorial waves as useful precursors to tropical cyclone occurrence and intensification. *Nature Communications*, 14, 511.

Ferrett, S., Methven, J., Woolnough, S.J., Yang, G.Y., Holloway, C.E. & Wolf, G. (2023) Hybrid dynamical-statistical forecasts of the risk of rainfall in South East Asia dependent on equatorial waves. *Monthly Weather Review*, 151, 2139–2152.

Ferrett, S., Yang, G.Y., Woolnough, S., Methven, J., Hodges, K. & Holloway, C.E. (2020) Linking extreme precipitation in south-east Asia to equatorial waves. *Quarterly Journal of the Royal Meteorological Society*, 146, 665–684.

Frank, W.M. & Roundy, P.E. (2006) The role of tropical waves in tropical cyclogenesis. *Monthly Weather Review*, 134, 2397–2417.

Fuchs-Stone, Z., Raymond, D.J. & Sentic, S. (2019) A simple model of convectively coupled equatorial Rossby waves. *Journal of Advances in Modeling Earth Systems*, 11, 173–184.

Gill, A.E. (1982) *Atmosphere–Ocean Dynamics*. San Diego: Academic Press.

Hersbach, H., Bell, B., Berrisford, P., Hirahara, S., Horanyi, A., Munoz-Sabater, J. et al. (2020) The ERA5 global reanalysis. *Quarterly Journal of the Royal Meteorological Society*, 146, 1999–2049.

Huffman, G.J., Stocker, E.F., Bolvin, D.T., Nelkin, E.J. & Tan, J. (2019) GPM IMERG final precipitation L3 half hourly 0.1 degree x 0.1 degree V06.

Inoue, K., Adames, A.F. & Yasunaga, K. (2020) Vertical velocity profiles in convectively coupled equatorial waves and the MJO: New diagnoses of vertical velocity profiles in the wavenumber-frequency domain. *Journal of the Atmospheric Sciences*, 77, 2139–2162.

Janicot, S., Mounier, F., Gervois, S., Sultan, B. & Kiladis, G.N. (2010) The dynamics of the West African monsoon. Part V: The detection and role of the dominant modes of convectively coupled equatorial Rossby waves. *Journal of Climate*, 23, 4005–4024.

Kemball-Cook, S. & Wang, B. (2001) Equatorial waves and air-sea interaction in the Boreal Summer Intraseasonal Oscillation. *Journal of Climate*, 14, 2923–2942.

Kiladis, G.N., Wheeler, M.C., Haertel, P.T., Straub, K.H. & Roundy, P.E. (2009) Convectively coupled equatorial waves. *Reviews of Geophysics*, 47, RG2003.

Knippertz, P., Gehne, M., Kiladis, G.N., Kikuchi, K., Satheesh, A.R., Roundy, P.E. et al. (2022) The intricacies of identifying equatorial waves. *Quarterly Journal of the Royal Meteorological Society*, 148, 2814–2852.

Latos, B., Lefort, T., Flatau, M.K., Flatau, P.J., Permana, D.S., Baranowski, C.B. et al. (2021) Equatorial waves triggering extreme rainfall and floods in southwest Sulawesi. *Indonesia Monthly Weather Review*, 149, 1381–1401.

Latos, B., Peyrille, P., Lefort, T., Baranowski, D.B., Flatau, M.K., Flatau, P.J. et al. (2023) The role of tropical waves in the genesis of Tropical Cyclone Seroja in the Maritime Continent. *Nature Communications*, 14, 856.

Matsuno, T. (1966) Quasi-geostrophic motions in the equatorial area. *Journal of the Meteorological Society of Japan*, 44, 25–42.

Matthews, A.J. (2021) Dynamical propagation and growth mechanisms for convectively coupled equatorial Kelvin waves over the Indian Ocean. *Quarterly Journal of the Royal Meteorological Society*, 147, 4310–4336.

Meehl, G.A., Lukas, R., Kiladis, G.N., Weickmann, K.M., Matthews, A.J. & Wheeler, M. (2001) A conceptual framework for time and space scale interactions in the climate system. *Climate Dynamics*, 17, 753–775.

Nakamura, Y. & Takayabu, Y.N. (2022a) Convective couplings with equatorial Rossby waves and equatorial Kelvin waves. Part II: Coupled precipitation characteristics. *Journal of the Atmospheric Sciences*, 79, 247–262.

Nakamura, Y. & Takayabu, Y.N. (2022b) Convective couplings with equatorial Rossby waves and equatorial Kelvin waves. Part I: Coupled wave structures. *Journal of the Atmospheric Sciences*, 79, 247–262.

Takayabu, Y.N. (1994) Large-scale cloud disturbances associated with equatorial waves. Part I: Spectral features of the cloud disturbances. *Journal of the Meteorological Society of Japan*, 72, 433–448.

Tsai, W.Y.H., Lu, M.M., Sui, C.H. & Lin, P.H. (2020) MJO and CCEW modulation on South China Sea and Maritime Continent boreal winter subseasonal peak precipitation. *Terrestrial, Atmospheric and Oceanic Sciences*, 31, 177–195.

Wheeler, M. & Kiladis, G.N. (1999) Convectively coupled equatorial waves: Analysis of clouds and temperature in the wavenumber-frequency domain. *Journal of the Atmospheric Sciences*, 56, 374–399.

Wheeler, M., Kiladis, G.N. & Webster, P.J. (2000) Large-scale dynamical fields associated with convectively coupled equatorial waves. *Journal of the Atmospheric Sciences*, 57, 613–640.

Yang, G.Y., Ferrett, S., Woolnough, S., Methven, J. & Holloway, C. (2021) Real-time identification of equatorial waves and evaluation of waves in global forecasts. *Weather and Forecasting*, 36, 171–193.

Yang, G.Y., Hoskins, B.J. & Slingo, J.M. (2003) Convectively coupled equatorial waves: A new methodology for identifying wave structures in observational data. *Journal of the Atmospheric Sciences*, 60, 1637–1654.

Yang, G.Y., Methven, J., Woolnough, S., Hodges, K. & Hoskins, B. (2018) Linking African easterly wave activity with equatorial waves and the influence of Rossby waves from the Southern Hemisphere. *Journal of the Atmospheric Sciences*, 75, 1783–1809.

Zhao, H. & Wu, L. (2018) Modulation of convectively coupled equatorial Rossby wave on the western North Pacific tropical cyclones activity. *International Journal of Climatology*, 38, 932–948.

How to cite this article: Matthews, A.J. (2025) A vorticity budget for theoretical and convectively coupled equatorial Rossby waves: Dynamical propagation and growth mechanisms. *Quarterly Journal of the Royal Meteorological Society*, 151:e4917. Available from: https://doi.org/10.1002/qj.4917